

# Simulated Extragalactic Observations with a Cryogenic Imaging Spectrophotometer

B.A. Mazin and R.J. Brunner

Department of Astronomy, The California Institute of Technology, MC 405-47, Pasadena,  
CA 91125

`bam@astro.caltech.edu,rb@astro.caltech.edu`

Received \_\_\_\_\_; accepted \_\_\_\_\_

Accepted by the Astronomical Journal

## ABSTRACT

In this paper we explore the application of cryogenic imaging spectrophotometers. Prototypes of this new class of detector, such as superconducting tunnel junctions (STJs) and transition edge sensors (TESs), currently deliver low resolution imaging spectrophotometry with high quantum efficiency (70–100%) and no read noise over a wide bandpass in the visible to near-infrared. In order to demonstrate their utility and the differences in observing strategy needed to maximize their scientific return, we present simulated observations of a deep extragalactic field. Using a simple analytic technique, we can estimate both the galaxy redshift and spectral type more accurately than is possible with current broadband techniques. From our simulated observations and a subsequent discussion of the expected migration path for this new technology, we illustrate the power and promise of these devices.

*Subject headings:* instrumentation: detectors — methods: statistical — galaxies: evolution

## 1. Introduction

In this paper, we discuss cryogenic imaging spectrophotometers (CIS), which appear to be the next major revolution in imaging technology. These devices simultaneously measure the energy, position, and arrival time of incoming photons with a spectral resolution  $R = \lambda/\Delta\lambda$  greater than 20 with high ( $> 50\%$ ) quantum efficiency. In addition to the improvements in the temporal resolution over CCDs, these new devices produce low resolution spectra which are collected without the need for filters, spanning a bandpass from the atmospheric cutoff at  $3100 \text{ \AA}$  to at least  $1 \text{ \mu m}$ . The red limit is imposed by blocking

filters designed to keep the rising sky flux from approaching the maximum count rate of the detectors — the devices have an inherent wavelength sensitivity out to around  $6\ \mu\text{m}$ . As a result, data collected from a cryogenic imaging spectrophotometer can be collected in 20% of the time as a conventional CCD and standard filter set (*e.g.*,  $u, g, r, i, z$ ), while simultaneously providing at least five times the spectral information.

The broad band nature of these detectors combined with their spectral resolution means that techniques designed for CCD photometry or conventional spectrometers are not optimum for these devices. For example, applying a magnitude limit in a specific passband can eliminate important data from consideration since an object faint in one passband may contain significant flux at other observed wavelengths. The four dimensional data cube returned by these devices (x position, y position, arrival time, and energy) presents new challenges in data reduction and analysis, which we address through simulated observations as discussed in Section 3.

Working CIS detectors for astronomy have recently been demonstrated in two forms: (1) Superconducting Tunnel Junction detectors (STJs: Perryman *et al.* 1999), and (2) Transition Edge Sensors (TESs: Romani *et al.* 1999). While these technologies deliver similar data to an observer, they have their own individual benefits and drawbacks, which we discuss in more detail in Section 2. Which of these detectors is expected to dominate in the future (if either — several promising new technologies have just emerged) is not clear, and will probably depend on which detector format is the first to produce an affordable, large format device.

As a simple example of the analysis of observations of a deep extragalactic field, we perform a spectral classification of the low resolution spectra generated by our simulated observations in Section 4. The simple  $\chi^2$  minimization approach we utilize, which is very similar to a template-based photometric redshift determination, provides a robust

estimation for both the galaxy redshift and spectral type. The significantly higher spectral resolution as compared to CCD observations (approximately five to ten times the spectral content) should enable the determination of additional parameters such as age and star formation rate with more advanced techniques such as a full eigen-spectra decomposition (*e.g.*, Connolly & Szalay 2000).

We conclude this paper with a discussion of the implications of this new detector technology on various areas of Astronomy (*cf.* Peacock *et al.* 1997), including space-based platforms such as the Next Generation Space Telescope (*NGST*). Throughout this paper we assume  $H_0 = 75 \text{ km s}^{-1} \text{ Mpc}^{-1}$  and  $\Omega_0 = 0.35$  unless otherwise noted.

## 2. Cryogenic Imaging Spectrophotometer Technology

Cryogenic superconducting detectors hold great promise as general purpose detectors for ground-based and space-based astronomy. However, several technical challenges must be addressed to make these detectors competitive for general use with current instrumentation.

The most severe problem is that current devices have low pixel counts. Innovative multiplexing solutions will be required to overcome this problem. Several multiplexing schemes are currently being tested, and plans are being made to build large format imaging spectrometers within the next several years.

These devices measure individual photons as pulses instead of storing charge in a potential well. This allows read noise free output and accurate timing resolution, but also implies a limited count rate and a high data rate for a large format array. A one megapixel device could produce uncompressed data rates approaching one Gigabyte per second or multiple Terabytes per night. Storing and analyzing this kind of data will present new challenges, and possibly require complete, on-line reduction.

In a cryogenic spectrophotometer the spectral resolution of the detectors is dependent on the operating temperature. Useful devices start working around 0.3 Kelvin. This means expensive He<sub>3</sub>, dilution, or adiabatic demagnetization refrigerators will be necessary.

Another problem is caused by the infrared background. Since these devices measure individual photons and are sensitive into the IR, thermal photons from the telescope and the atmosphere can create a low level background photon flux which degrades the spectral resolution of the detectors. Special blocking filters that thoroughly attenuate the thermal IR will be needed for these devices to reach their full potential from the ground.

## 2.1. Transition Edge Sensors

Transition edge sensors work by holding a small piece of superconductor at its transition temperature by means of electrothermal feedback. An incoming photon warms up the detector, and this causes a decrease in the power needed to maintain the superconductor at its transition temperature. This current deficit pulse is read out by a Superconducting Quantum Interference Device (SQUID) array.

The TES can ultimately achieve slightly higher spectral resolution than current generation STJs, but it does have its drawbacks. The pixel size is limited by the heat capacity of the superconductor. Current TES devices are 18 $\mu$ m square (Romani *et al.* 1999). The SQUID readout, however, cannot be shrunk to much more than 100 $\mu$ m on a side. This means that unless powerful multiplexing schemes (*e.g.*, Chervenal *et al.* 1999) are developed a TES will have a low filling factor and need a complex and expensive readout for each pixel. The spectral resolution of a TES depends on its base temperature (currently  $\sim$  40 mK), so high spectral resolution comes at the price of a very complex cooling apparatus. Despite these challenges, the TES represent the only current CIS technology

that has the clear potential to achieve spectral resolution greater than approximately 60 at 3000 Å.

## 2.2. Superconducting Tunnel Junction Detectors

Superconducting tunnel junction detectors work by absorbing a photon in a strip of superconductor (usually Tantalum) held well below its transition temperature. The incoming photon breaks up Cooper pairs and creates free charge carriers called quasiparticles. The quasiparticles diffuse through the Tantalum strip and are trapped in Al-Al<sub>2</sub>O<sub>3</sub>-Al Josephson junctions on each end. The junctions are connected to either a low noise amplifier or a RF-SET (radio frequency single electron transistor, see Schoelkopf *et al.* 1997). Since the charge created by the photon is distributed over both junctions, the amount of charge read out in each junction determines the location the photon hit, and the total charge determines the photon energy. The ultimate spectral resolutions of a STJ is limited by the intrinsic scatter in the number of quasiparticles created by a photon of a given energy. This is known as the Fano limit and is a function of the superconducting energy gap of the material used for the absorber. For a Tantalum absorber this works out to approximately 55 at 3000 Å and decreases at longer wavelengths as the square root of the photon energy to 30 at 10000 Å.

STJs have their own unique limitation. Most designs use back tunneling in the junctions to increase the signal strength. This, along with the shot noise associated with the bias current, lowers the effective spectral resolution. The Josephson current in each junction must be highly suppressed by a magnetic field, thus very uniform junctions are needed so that a magnetic field will suppress every junction.

The charge division provided by having two junctions on one absorber provides STJs

with an inherent imaging capability - the number of virtual pixels on one strip is comparable to the spectral resolution (Kraus *et al.* 1989). For imaging cameras this means many more pixels per readout, a real advantage for practical designs.

### 3. Simulated Observations

In order to demonstrate observations with a cryogenic imaging spectrophotometer, we have generated a simulated extragalactic field. This operation is complicated by the fact that a CIS essentially acts as a low resolution spectrograph and we therefore need not only a simulated galaxy catalog, but also the corresponding spectra for each source. In the following sections, we detail the relevant steps required to generate the simulated data, tracing the photons path from the extragalactic source to the detector. We will address the more complicated issues of star/galaxy separation, blending, extended sources, and the identification of active galaxies in subsequent papers.

#### 3.1. Galaxy Catalog

Since we are primarily concerned with demonstrating the utility of CIS detectors, and not in generating accurate cosmological simulations, we have used an existing simulated galaxy catalog. In particular, we started with a galaxy catalog that was drawn from an NGST cosmological simulation ( $\Omega = 0.35$ ,  $H_0 = 75$ , Open CDM) performed by Myungshin Im (Im *et al.* 2000). This simulation covers a  $2' \times 2'$  area, which, for our purposes, is incidental (we are not simulating the full three-dimensional data cube, only the individual sources). This catalog includes the galaxy morphological type, redshift, and  $I$  and  $K$  apparent magnitudes. These parameters were used to generate spectra for each galaxy in the data set.

We restricted our sample to only include galaxies with  $19 \leq I \leq 28$ , as galaxies with  $I < 19$  are expected to exceed the maximum count rate of a typical detector, while galaxies with  $I > 28$  will provide an insufficient signal for later analysis. As a result, our final galaxy catalog contains 449 Elliptical galaxies, 4077 Spiral galaxies, and 4192 Irregular galaxies. The resulting redshift distributions for each spectral type in the catalog is shown in Figure 1.

### 3.2. Model Spectra

As morphological type is a poorly defined concept at higher redshift, we interpreted the galaxy types from the original cosmological simulation as representative of different star formation histories. We defined the transformation as follows: Ellipticals are simulated by an instantaneous burst of star formation with subsequent passive evolution, Spirals are simulated with an exponentially decaying star formation rate ( $\tau = 1$  Gyr), and Irregulars are simulated with a constant star formation rate.

The actual model spectra were constructed using the GISSEL software (Bruzual and Charlot 1998). The Elliptical and Spiral galaxy models were generated at ages of 1, 2, 5, 10, and 15 Gyr with solar metallicity and a Salpeter IMF. Irregulars were assumed to be inherently young and only one model was generated. For each galaxy in the simulated catalog an age was determined based on its redshift and our assumed cosmology. Using this age we selected the closest matching model spectra. Traces of the complete set of the input model spectra used can be found in Figure 2.

After selecting the appropriate model spectra, we apply various corrections in order to account for different attenuation factors that affect the emitted photons. The first modification (which is optional, in our analysis we simulate observations with and without



this complication) is a correction for cosmological variance (or template incompleteness). Template incompleteness results when the template spectra used to fit the observed data do not span the entire range of possible galaxy spectra. This problem is addressed in template-based photometric redshift estimation by including many templates with various dust extinction, stellar populations, *etc.*, which reduces the contribution of template incompleteness (*e.g.*, Sawicki *et al.* 1996).

Template incompleteness was simulated by adding a single, random component of stellar light, according to the following likelihood rule: 25% O stars, 50% A stars, 20% G stars, and 5% M stars. The actual stellar spectra were drawn from a published stellar library (Pickles 1998), scaled by a Gaussian random number with a sigma of 5% of the amplitude of the model galaxy spectra, and added to the original galaxy model spectra.

To account for dust in the simulated galaxies, the model spectra were attenuated using an empirical extinction law (Calzetti *et al.* 1994). The actual extinction parameters for the models with cosmic variance were randomly selected according to a Gaussian probability distribution function with mean and sigma determined by the following rules:  $E(B - V) = 0.0 \pm .01$  for Ellipticals,  $E(B - V) = 0.1 \pm .02$  for Spirals and  $E(B - V) = 0.3 \pm .05$  for Irregulars (Calzetti *et al.* 1994). The models without cosmic variance used the mean values described above with no random component. In order to avoid unphysical attenuation, the extinction parameters are restricted to positive values.

Following the dust correction, the spectra were redshifted and corrected for the mean attenuation due to the inter-galactic medium (Madau *et al.* 1996). Each spectrum was normalized by defining the measured apparent  $K$  magnitude to be equal to the original  $K$  magnitude from the cosmological simulations. An SDSS  $i'$  magnitude was then computed for each galaxy. The final steps in the spectral simulator are to apply the necessary corrections for the estimated atmospheric extinction and the combined telescope and device quantum

efficiencies (in this particular simulation we utilize the expected quantum efficiency for an STJ, see Rando *et al.* 1997, and assume a 40% loss of photons in the telescope and camera optics). A detailed, graphical outline of these steps is shown in Figure 3.

### 3.3. Broadband Photometric Redshifts

In order to test the validity of our models and compare them quantitatively to similar work in the literature we computed broad band photometric redshifts using our galaxy catalog and associated model spectra. This was accomplished by simulating a wide field image from the Keck telescope with one hour of integration time in each of four visible bands,  $U, G, R, i'$ . For each galaxy a magnitude and its associated photometric errors were produced. Using the same  $\chi^2$  template fitting technique described in Section 4 we fit all galaxies with photometric errors of less than  $0.1^m$  (*i.e.* 10 % photometry) in each observed band. The resulting redshift errors,  $z_{real} - z_{phot}$  were then used to determine the standard deviation of the redshift error,  $\sigma_z$ . In Table 1, these results are compared to results of simulations by Bolzonella *et al.* (2000) using a similar filter set and the results of Lanzetta *et al.* (1999) using a combination of HST photometry and ground based near-infrared photometry.

It is clear from these simulations that our method of simulating template incompleteness does in fact broaden the computed redshift distribution to levels comparable (even slightly higher) than found in the literature. The redshift range where we have the greatest differences with existing broad band data is  $z < 1.0$ , where our errors are dominated by irregular galaxies with poor photometry. As our set of galaxy spectral templates only includes one Irregular, we are clearly experiencing the effects of template incompleteness as we do not properly identify those irregular galaxies with significant flux from late type stars.

### 3.4. Detector Simulations

Each of the resultant galaxy spectra were pushed through a custom developed STJ simulator at two spectral resolutions,  $R = 20$  at  $3000 \text{ \AA}$  and  $R = 55$  (Fano-limited) at  $3000 \text{ \AA}$  with  $R$  decreasing as  $1/\sqrt{\lambda}$ . This STJ simulator uses the input spectrum to perform a photon by photon simulation of the output of the STJ assuming a one hour integration on the Keck Telescope in  $0.6''$  seeing. The dominant noise source is sky noise, which is simulated with the STJ simulator using the sky spectrum of Turnrose (1974). Figure 4 displays sample output of the STJ simulator.

Our analysis method simulates aperture photometry with a  $1''$  diameter circular aperture. Depending on the seeing conditions and the actual galaxy diameter, a variable size aperture (*i.e.* a “total” magnitude) could yield a higher signal to noise ratio. The imaging properties of the CIS detector will allow observers to dynamically select the best aperture during data reduction, or to allow spectrophotometry on each individual pixel. The latter, for example, could yield interesting data for extended sources on the differences in age, metallicity, and dust content of the stellar populations of bulges compared to disks.

The broad band nature of these simulated observations makes conventional selection criteria like an  $i'$  band magnitude limit difficult to apply. We propose that a correct formalism is to utilize the broad band signal to noise ratio ( $S/N$ ). This is just the total detected source counts divided by the estimated noise produced by the object plus sky Poisson noise. This selection criteria does not translate well into a magnitude limited sample since an object that is faint in one band may provide significant flux at other wavelengths that the CIS detector is observing. It does, however, quantify the low-resolution spectral signal generated by the CIS detector. Careful analysis will be needed to quantify the selection effects introduced by this formalism. The bottom panel in Figures 7, 8, and 9 shows the locations of the simulated galaxies in a two-dimensional broad band  $S/N$  ratio

and SDSS  $i'$  band apparent magnitude phase space.

#### 4. Data Analysis

With the advent of the Hubble Deep Field (Williams *et al.* 1996), the utility of estimating redshifts from broadband photometry has achieved wide-spread acknowledgment. Several complementary approaches have been developed, including techniques which use an empirically derived function of galaxy flux or colors (Connolly *et al.* 1995; Brunner *et al.* 1997; Brunner 1997; Brunner *et al.* 1999) and spectral template techniques which minimize the difference between redshifted empirical or model templates and the observed photometry to determine redshifts (Gwyn & Hartwick 1996; Lanzetta *et al.* 1996; Mobasher *et al.* 1996; Sawicki *et al.* 1996). All of these techniques, however, are designed to utilize broadband photometry, not low resolution spectra, and they do not, as a result, extract the maximal amount of information from our simulated data. Since the major intent of this paper is not to develop a theoretical framework for maximal data extraction from CIS observations (which we defer to a subsequent paper), we instead develop a technique for determining galaxy parameters which is similar to template photometric redshift estimation.

In order to determine the redshift of the simulated galaxies, a subset of the initial model spectra were used. The following six model templates were deemed to sufficiently span the template space occupied by the simulated galaxies: 2 Gyr Elliptical, 10 Gyr Elliptical, 2 Gyr Spiral, 5 Gyr Spiral, 10 Gyr Spiral, and Irregular. The model spectra were attenuated as described in the previous section to generate a series of template spectra with no cosmic variance. A grid of new template spectra were generated by redshifting these six model spectra over the range  $0 \leq z \leq 5$  with  $\Delta z = 0.025$ . The new spectra were convolved with a Gaussian kernel to simulate the effects of an STJ with a spectral resolution  $R = 20$  and  $R = 55$  at  $3000 \text{ \AA}$ . The resulting smoothed spectrum was rebinned into  $100 \text{ \AA}$  bins to

match the output of the simulator.

The best fit was determined by finding which template minimized a  $\chi^2$  error statistic (Press *et al.* 1992). Examples of the fit returned by this algorithm are shown in Figures 5 and 6. This method returns both the galaxy spectral type and redshift. The measured deviation for all galaxy types is shown in Figures 7, 8, and 9. The results for the  $R = 55$  simulations, as well as the lower resolution  $R = 20$  simulation are summarized in Table 2. Adjusting the minimum  $S/N$  ratio used by the fitting algorithm showed that a  $S/N$  ratio of 30 is adequate to provide an accurate redshift. Lower  $S/N$  ratios can cause misidentifications because of noise spikes.

Clearly, as expected, our simple technique operates most effectively when there is no cosmic variance in our simulated observations (in which case we do not suffer from template incompleteness). Furthermore, as expected, the results for the higher resolution STJ detector are considerably better than the equivalent results for the lower resolution detector (see Table 2).

For Elliptical galaxies, our naive approach does a good job at determining the best redshift and spectral template, except for some outliers in the simulations which include cosmic variance. A quick comparison of the simulations with and without cosmic variance for those Elliptical galaxies which are detected with  $S/N$  above 30 shows that the small number of outliers increase the dispersion in the redshift estimation by an order of magnitude. Upon closer inspection, these simulated galaxies invariably had significant contributions of blue stellar light added to their spectrum (similar to an E+A galaxy). Since there is no comparable template spectrum in our sample (*i.e.* no E+A template) to model this type of galaxy, our fitting algorithm misidentifies these cases. Aside from these rare exceptions, the dispersion in the estimated redshift versus the simulated redshift for Ellipticals is lower than for the other galaxy types. We attribute this to the greater relative

Table 1. A comparison of the rms dispersion in the estimated photometric redshifts for template-based photometric redshifts using space based data (Lanzetta *et al.* 1999), ground-based simulations (Bolzonella *et al.* 2000), and our no cosmic variance and cosmic variance simulations. For both the ground-based calculations and our own simulations, we present the dispersion calculations at both 10 and 5 percent photometric limits.

Redshift Range	Space Based	Ground Based		No Variance		Variance	
		10%	5%	10%	5%	10%	5%
$0.0 < z < 1.0$	0.1	0.15	0.12	0.27	0.15	0.48	0.39
$1.0 < z < 2.0$	0.1	0.35	0.26	0.21	0.09	0.40	0.39
$z > 2.0$	0.3	0.28	0.19	0.12	0.02	0.29	0.14

Table 2. The dispersion in the estimated redshifts for the different simulation parameters (spectral resolution and the inclusion of cosmic variance) for each of the different star formation histories at broadband  $S/N$  ratios of 15 and 30.

Spectral Resolution	Cosmic Variance	Elliptical		Spiral		Irregular	
		15	30	15	30	15	30
20	No	0.2157	0.0474	0.1110	0.0578	0.2929	0.1750
55	No	0.0730	0.0111	0.1930	0.0422	0.2715	0.1326
20	Yes	0.2923	0.2462	0.1909	0.1008	0.4622	0.3967
55	Yes	0.1779	0.1386	0.1764	0.0433	0.4544	0.3444

strength of the spectral breaks in the instantaneous burst models compared to the younger star forming models.

Another interesting but rare situation arises for a small number of Irregular galaxies in the cosmic variance simulations, in which the redshift is systematically misidentified. This problem is illustrated in Figure 10 where high  $S/N$  irregulars show a much larger dispersion than other galaxy types at similar magnitudes. This problem was also evident in the broad band simulations discussed in Section 3.3. In these special cases, low redshift Irregulars are confused with young  $z \sim 1.5$  Spiral and Irregular templates. These are mainly detections which contain a significant component of late type stellar light added by the cosmic variance routine. Since a young Irregular is likely to be dominated by O and B stars, our method for adding cosmic variance can easily overestimate the likely contribution of late type stars. In a real observation this problem could be corrected by adding a template with a small contribution of late type stellar light. This means we expect a more realistic deviation of Irregulars to be closer to that predicted by the models with no cosmic variance.

The simulated galaxies in the special cases described above are all misclassified as a result of template incompleteness. When the  $S/N$  ratio in these galaxies is over about 30, it is possible to determine which galaxies are effected by template incompleteness by monitoring the  $\chi^2$  goodness of fit parameter (Press *et al.* 1992). Selecting and eliminating these galaxies from consideration based on this parameter would lower the deviation much closer to the simulated galaxies with no cosmic variance. However, in a real observation, the fact that these galaxies do not conform to the standard galaxy models would make them interesting targets for further study.

One last peculiarity in the measured deviation (somewhat independent of broadband  $S/N$  cut or inclusion of cosmic variance) is the increase in the dispersion of the relationship for Spiral and Irregular galaxies with  $1 \leq z \leq 2$ . This redshift region is a problem for

both photometric and spectroscopic redshift estimation due to the dearth of spectroscopic features. As a result, galaxies encounter problems due to template confusion. A possible solution to this problem may be obtained by improving our template set, but it seems likely that the only real solution is to expand the wavelength coverage of the detectors into the near-infrared. In the latter scenario, the 4000 Å break would continue to be sampled on the red side of the spectrum to sufficiently high redshifts that we would eventually begin to simultaneously sample the rest frame UV features like the Lyman break on the blue side of the spectrum. We discuss several ways of increasing the wavelength coverage below.

Since the templates were generated on a grid with a spacing of  $\Delta z = 0.025$  the maximum error in our redshift estimation due to grid quantization is 0.0125. If we assume this error is randomly distributed, the best we can do is a deviation of 0.0063. This systematic error is over 50% of our best case dispersion (see Table 2), suggesting that our results can be significantly improved with more advanced spectral classification techniques.

Overall, we expect that with real data and a large template set (theoretical or empirical), it will be possible to obtain deviations close to those computed in our simulations with no cosmic variance. If we ignore the problem area between  $z = 1.2$  and  $z = 1.6$  this gives us an expected deviations of less than 0.06 for all galaxy types with  $z < 5$ . With the addition of cosmic variance the deviation is broadened to 0.16, which should be considered an upper limit. These values can be compared with Table 1, which shows that this one ground based detector can determine redshifts far more accurately than is possible with the best current techniques using Hubble Deep Field photometry and deep Keck IR images.



## 5. Discussion

These simulations clearly show that cryogenic spectrophotometers will be far more efficient and accurate than any broad band technique for redshift determination. The attraction of these detectors is obvious. The minimal five-fold reduction in observing time that is possible by removing the filters from conventional photometry is equivalent to transforming the Keck telescope into a 22 meter telescope for a cost which is considerably lower than building such a telescope.

From these simulations, it is possible to directly compare the efficiency of this detector to broadband techniques. In our most accurate broadband simulation we identify 1018 out of 8717 galaxies with the highest detected redshift around 3 using 4 hours of observation time with Keck. The CIS detector with  $R = 55$  and  $S/N > 30$  identifies 2045 galaxies much more accurately in only one hour out to a redshift of 5, translating into an 8 fold efficiency increase. This advantage, however, is only realized in detectors of the same size. Since CCDs currently are very big, CIS detectors will become competitive for large galaxy redshift surveys when their pixel counts reach around 1/10 those of CCDs.

We expect that if large format CIS detectors can be built and made economical they will eventually replace CCDs as the wide field detectors of choice at most observatories. The consequences for using these devices in space is even more dramatic. Due to the removal of atmospheric effects, space-based CIS devices would allow imaging spectrophotometry from 1100 Å to 6  $\mu\text{m}$  with the same detector. A large field imager of this type, mounted on a *NGST*-class telescope with passively cooled mirrors and actively cooled detectors, would allow images of similar depth to the Hubble Deep Field with 2% of the observation time required with the WFPC2 instrument, and significantly higher spectral coverage and resolution. Significant performance gains can also be achieved by putting the ground-based detector behind an adaptive optics (AO) system. This would lower the background count

rate enough to allow wavelength coverage out to  $2.5 \mu\text{m}$  with diffraction limited imaging in the near-infrared.

There are many other possible astronomical applications to this technology. Applications like an order sorter for an echelle spectrograph, optical pulsar and X-ray binary work, speckle imaging, interferometry, integral-field spectroscopy, and lensing surveys are certainly possible and interesting projects, but only scratch the surface of the potential uses. In general, almost any project which uses multicolor photometry on faint sources will be better served by large format CIS arrays.

The techniques used in this paper for redshift estimation are not particularly sophisticated. Indeed, we expect that spectral classification techniques may prove to be more robust, as well as extracting more information from the low resolution spectral energy distributions provided by these detectors.

## 6. Conclusions

In this paper, we have discussed the different types of Cryogenic Imaging Spectrophotometers which are under development, including Superconducting Tunnel Junction detectors and Transition Edge Sensors. We have presented simulated observations of a deep extragalactic field using a custom developed STJ simulator. While purposefully ignoring stars and active galaxies in order to focus the analysis, we have demonstrated that cryogenic spectrophotometers are an extremely promising new technology for extragalactic astronomy. Future work in this area will include more detailed simulations of extragalactic fields including stars and active galaxies, and observations based from the ground and from space. More advanced spectral analysis techniques will also be developed to maximally extract information from the available data.

We are grateful to Pat Cote, Lori Lubin, Brian Kern, Chris Martin, David Schminiovich, and Todd Small for useful discussions. More information on STJ detectors is available at <http://spaceball.caltech.edu/>.

## REFERENCES

- Bolzonella, M., Miralles, J., & Pello, R. A&A, in press
- Brunner, R.J 1997, PhD. Thesis, The Johns Hopkins University.
- Brunner, R.J, Connolly, A.J., Szalay, A.S., & Bershad, M.A. 1997, ApJ, 482, L21.
- Brunner, R.J, Connolly, A.J., & Szalay, A.S. 1999, ApJ, 516, 563.
- Bruzual, G.A., & Charlot, S. 1998, ApJ, private communication.
- Calzetti, D., Kinney, A.L., & Storchi-Bergmann, T. 1994, ApJ, 429, 582.
- Chervenak, J.A., Irwin, K.D., Grossman, E.N., Martinis, J.M., Reintsema, C.D., & Huber, M.E. 1999, *Appl. Physics Letters*, 74, 4043.
- Connolly, A.J., Csabai, I., Szalay, A.S., Koo, D.C., Kron, R.G., and Munn, J.A. 1995, AJ, 110, 6.
- Connolly, A.J. & Szalay, A.S., AJ, 117, 2052.
- Gwyn, S.D.J., & Hartwick, F.D.A 1996, ApJ, 440, 470.
- Im, M., *et al.* 2000, in preparation.
- Kraus, H., *et al.* 1989, *Physics Letters B*, 231, 195.
- Lanzetta, K.M., Yahil, A., & Fernandez-Soto, A. 1996, Nature, 381, 759.
- Lanzetta, K.M., Chen, H., Fernandez-Soto, A., Pascarelle, S., Puetter, R., Yahata, N., & Yahil, A. 1999, in *Photometric Redshifts and High-Redshift Galaxies*, ASP conference series, volume 191, Eds. R. Weymann, L. Storrie-Lombardi, M.Sawicki & R. Brunner.

- Madau, P., Ferguson, H.C., Dickinson, M.E., Giavalisco, M., Steidel, C.C., & Fruchter, A. 1996, *MNRAS*, 283, 1388.
- Mobasher, B., Rowen-Robinson, M., Georgakakis, A., & Eaton, N. 1996, *MNRAS*, 282, L7.
- Peacock, A., Verhoeve, P., Rando, N., Perryman, M. A. C., Taylor, B. G., Jakobsen, P. 1997, *A & AS*, 123, 581.
- Perryman, M.A.C., Favata, F., Rando, N., & Taylor, B.G. 1999, *A&A*, 346, L30.
- Pickles, A.J. 1998, *PASP*, 110, 863.
- Press, W.H., Teukolsky, S.A., Vetterling, W.T., & Flannery, B.P. 1992, *Numerical Recipes in C*, Cambridge University Press, 2 edition.
- Rando, N., Andersson, S., Collaudin, B., Gondoin, P., Verveer, J., Verhoeve, P., den Hartog, R., Venn, R., Salmi J. & Peacock, A. 1997, *Proc. of LTD-7*, Munich 1997, p101.
- Romani, R. W., Miller, A.J., Cabrera, B., Figueroa-Feliciano, E., & Nam, S. W. 1999, *ApJ*, 521, L153.
- Sawicki, M.J., Lin, H., & Yee, H.K.C. 1997, *AJ*, 113, 1.
- Schoelkopf, R.J., Wahlgren, P., Kozhenikov, A.A., Delsing, P., & Prober, D.E. 1997, *Science*, 280, 1238.
- Turnrose, B.T. 1974, *PASP*, 86, 545.
- Williams, R.E., Blacker, B., Dickinson, M.E., Dixon, W., Ferguson, H.C., Fruchter, A.S., Giavalisco, M., Gilliland, R.L., Heyer, I., Katsanis, R., Levay, Z., Lucas, R.A., McElroy, D.B., Petro, L., Postman, M., Adorf, H., & Hook, R. 1996, *AJ*, 112, 1335.

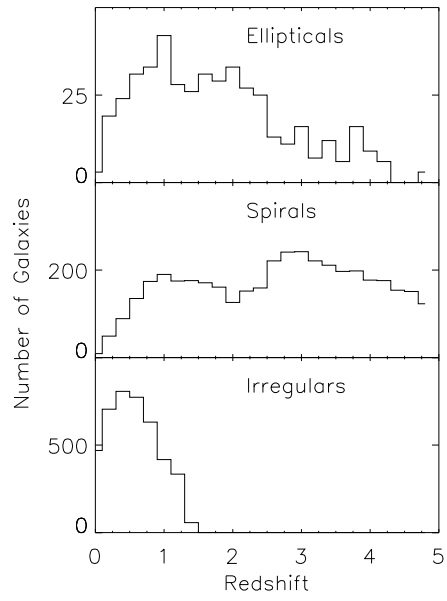


Fig. 1.— Redshift distribution of the three types of galaxies in the catalog.

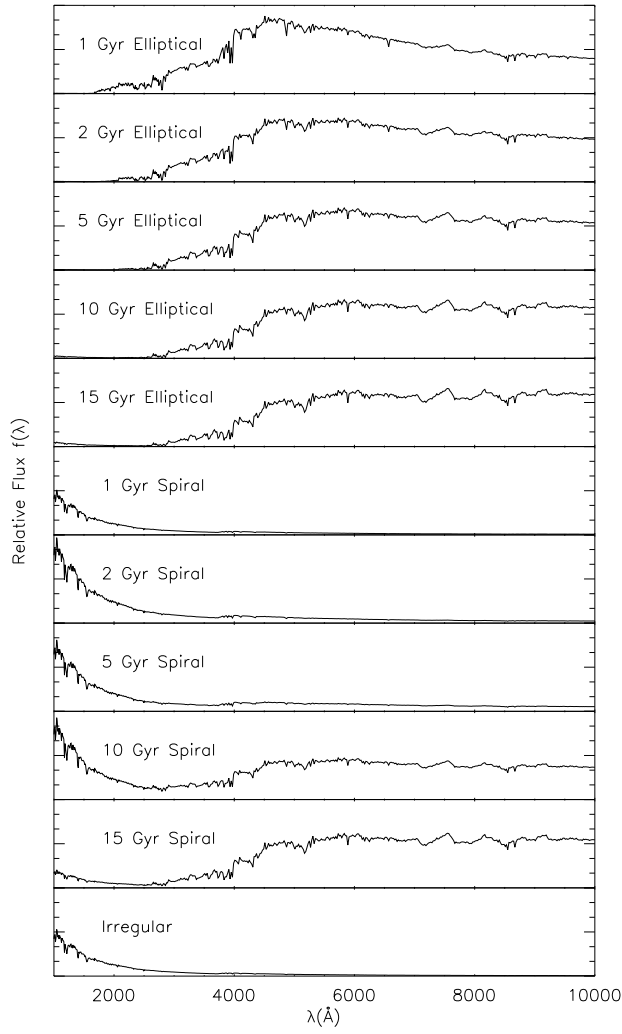


Fig. 2.— The normalized flux of the starting model spectra used to simulate the galaxy catalog.

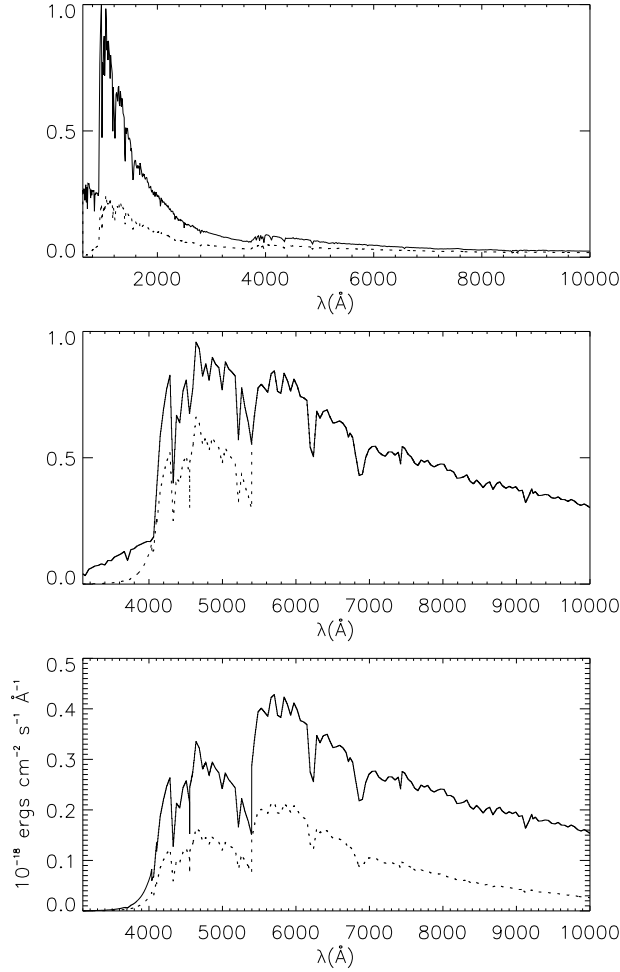


Fig. 3.— Attenuation steps used to generate the spectral energy distributions of the input models to the STJ simulator. A  $z = 3.44$  spiral is simulated in the above panels. The top panel contains the initial Bruzual and Charlot (1998) model as a solid line. The dotted line shows the effect of dust attenuation ( $E(B - V) = .1$ ) in the galaxy. The solid line in the center panel shows the redshifted spectra, and the dotted line in the center panel shows the effects of IGM attenuation. The solid line in the bottom panel shows the normalized spectra ( $m_K = 23.88$ ). The dotted line in the bottom panel shows the final model after accounting for atmospheric attenuation and device quantum efficiency.



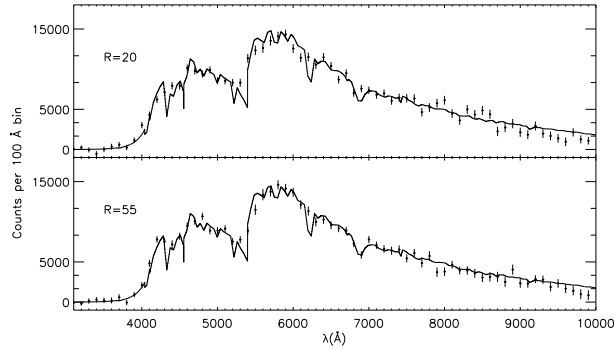


Fig. 4.— Output of the STJ simulator based on the input spectrum from Figure 3. This is a simulated spectra of a  $z=3.44$  spiral with  $m_K = 23.88$  observed for one hour on Keck with  $0.6''$  seeing at  $R = 20$  and  $55$ . The solid line is the spectrum computed in Figure 3. The dots represent the number of counts in each  $100 \text{ \AA}$  wide bin with their estimated errors. This galaxy is detected with a broadband signal to noise ratio of 100.

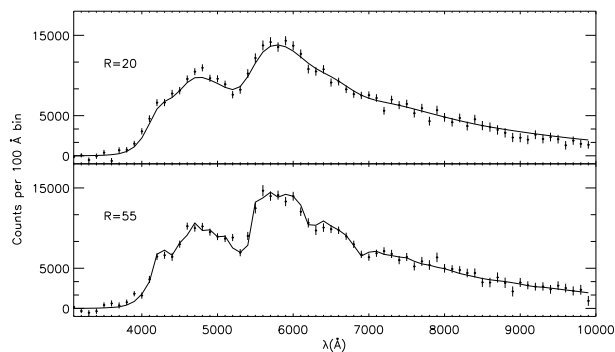


Fig. 5.— The best fit template (2 Gyr spiral at  $z = 3.45$ ) generated by the redshift estimation algorithm for the simulated STJ spectrum shown in Figure 4.

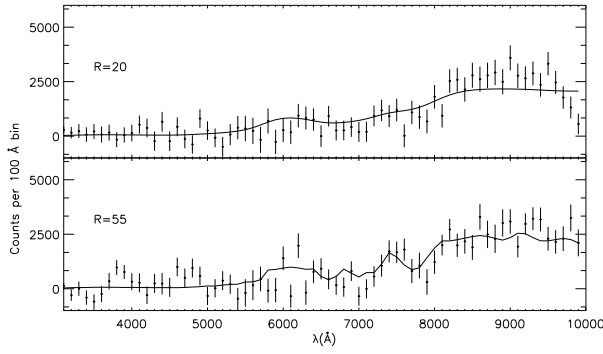


Fig. 6.— A simulated Elliptical at  $z = 1.805$  with  $m_K = 21.74$  and  $m_{i'} = 26.05$ , detected with a  $S/N$  ratio of 17 (which is below our nominal  $S/N$  cut). The redshift estimation algorithm determined the best fit template to this galaxy was a 2 Gyr elliptical at  $z = 1.725$  which is shown as the solid line.

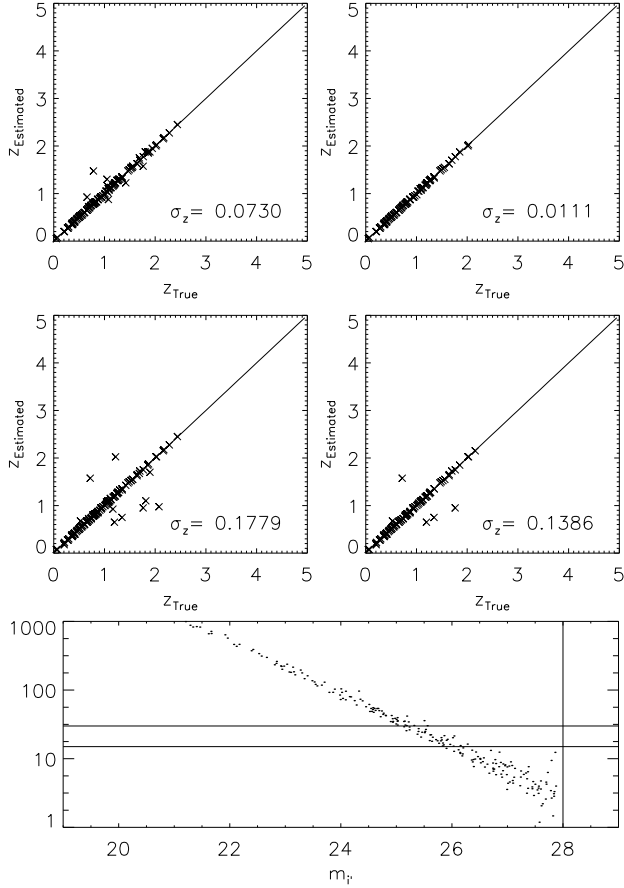


Fig. 7.— The true versus estimated redshift for the simulated Elliptical galaxies observed with a  $R = 55$  STJ detector on Keck for one hour. The top row contains the simulations without the effects of cosmic variance. The second row contains simulations with all of the attenuation factors, including cosmic variance. In the first column the fitting algorithm fits all galaxies with a broadband  $S/N$  ratio greater than 15, while the second column uses a minimum  $S/N$  ratio of 30. The bottom panel shows the distribution of broad band  $S/N$  ratio versus SDSS  $i'$  magnitude with the horizontal lines representing the  $S/N$  cuts described previously.

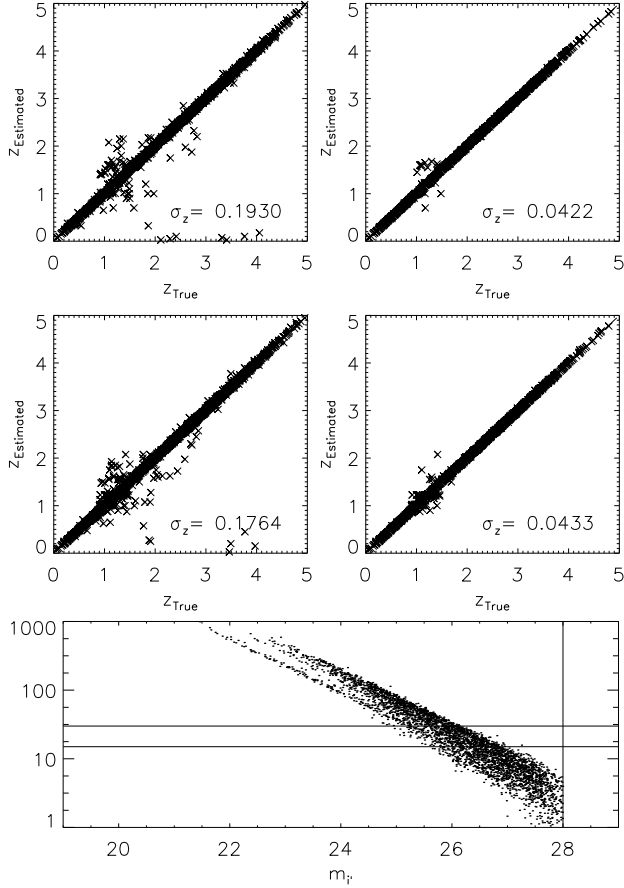


Fig. 8.— The true versus estimated redshift for the simulated Spiral galaxies observed with a  $R = 55$  STJ detector on Keck for one hour. The top row contains the simulations without the effects of cosmic variance. The second row contains simulations with all of the attenuation factors, including cosmic variance. In the first column the fitting algorithm fits all galaxies with a broadband  $S/N$  ratio greater than 15, while the second column uses a minimum  $S/N$  ratio of 30. The bottom panel shows the distribution of broad band  $S/N$  ratio versus SDSS  $i'$  magnitude with the horizontal lines representing the  $S/N$  cuts described previously.

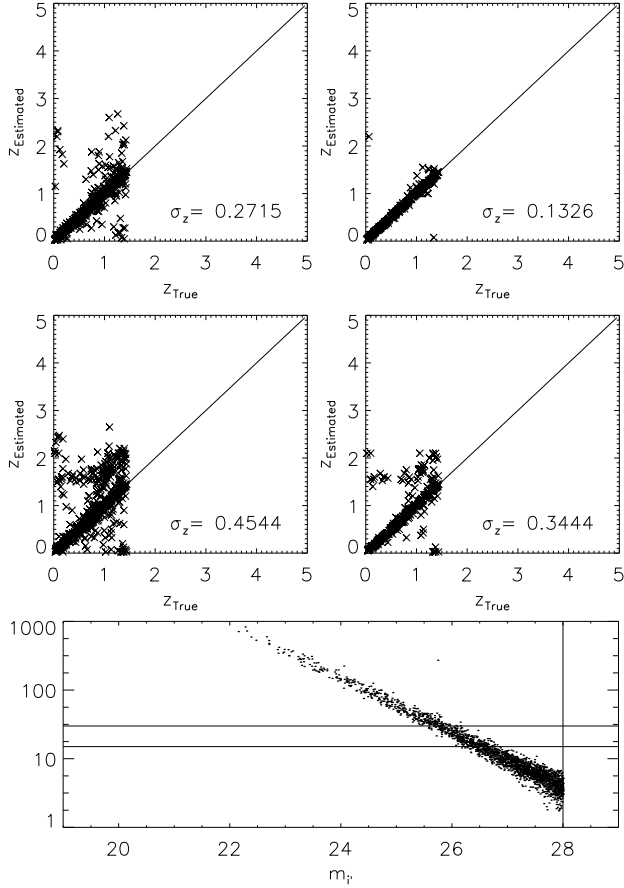


Fig. 9.— The true versus estimated redshift for the simulated Irregular galaxies observed with a  $R = 55$  STJ detector on Keck for one hour. The top row contains the simulations without the effects of cosmic variance. The second row contains simulations with all of the attenuation factors, including cosmic variance. In the first column the fitting algorithm fits all galaxies with a broadband  $S/N$  ratio greater than 15, while the second column uses a minimum  $S/N$  ratio of 30. The bottom panel shows the distribution of broad band  $S/N$  ratio versus SDSS  $i'$  magnitude with the horizontal lines representing the  $S/N$  cuts described previously.

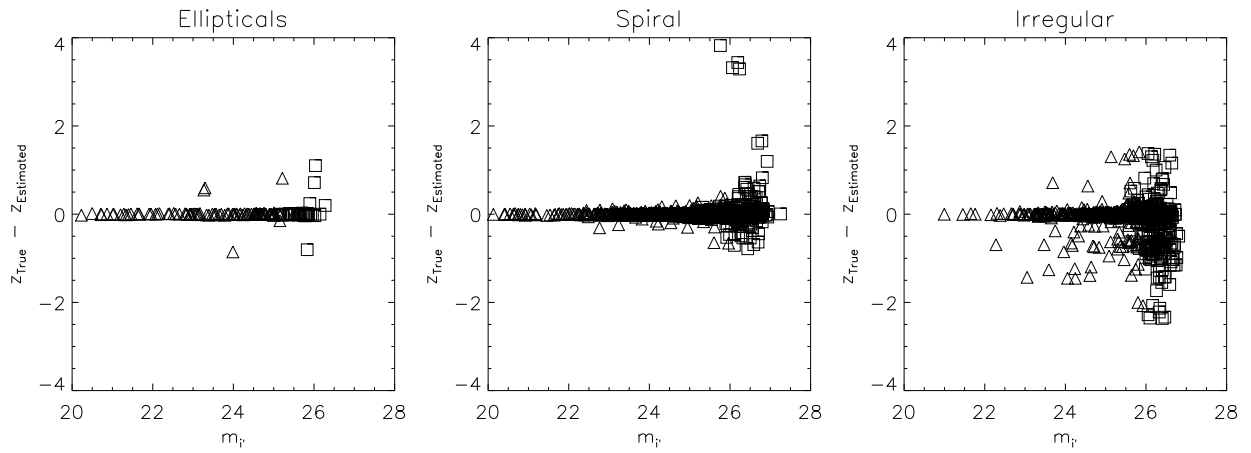


Fig. 10.— The deviation,  $z_{True} - z_{Estimated}$ , of our simulated galaxies with cosmic variance compared with their SDSS  $i'$  magnitude. Galaxies detected with a  $S/N$  between 15 and 30 are represented by boxes. Galaxies detected with a  $S/N$  greater than are 30 represented by triangles.